

BattX: An equivalent circuit model for lithium-ion batteries over broad current ranges

Nikhil Biju, Huazhen Fang*

Department of Mechanical Engineering, University of Kansas, Lawrence, KS 66045, USA

ARTICLE INFO

Keywords:

Lithium-ion batteries
Battery modeling
Equivalent circuit model
Electrochemical model
High-power battery systems

ABSTRACT

Advanced battery management is as important for lithium-ion battery systems as the brain is for the human body. Its performance is based on the use of fast and accurate battery models. However, the mainstream equivalent circuit models and electrochemical models have yet to meet this need well, due to their struggle with either predictive accuracy or computational complexity. This problem has acquired urgency as some emerging battery applications running across broad current ranges, e.g., electric vertical take-off and landing aircraft, can hardly find usable models from the literature. Motivated to address this problem, we develop an innovative model in this study. Called *BattX*, the model is an equivalent circuit model that draws comparisons to a single particle model with electrolyte and thermal dynamics, thus combining their respective merits to be computationally efficient, accurate, and physically interpretable. The model design pivots on leveraging multiple circuits to approximate major electrochemical and physical processes in charging/discharging. Given the model, we develop a multipronged approach to design experiments and identify its parameters in groups from experimental data. Experimental validation proves that the *BattX* model is capable of accurate voltage prediction for charging/discharging across low to high C-rates.

1. Introduction

Lithium-ion batteries (LiBs) are a key power source for consumer electronics, electrified transportation, smart grids, and renewable energy. Compared with alternative secondary storage sources, they provide a set of outstanding characteristics, including high energy/power density, high nominal voltage, no memory effect, low self-discharge rates, and long cycle life [1–3]. Recent technological advances have further improved their power delivery and cost efficiency for a wider application spectrum. High-quality dynamic models are fundamental to the monitoring and control of LiBs to ensure operational safety and performance. While the growing research has led to a variety of useful models, the literature still lacks fast and accurate models for applications involving charging/discharging from low to high current rates. To fill this gap, we propose a first-of-its-kind equivalent circuit model named *BattX* and demonstrate its predictive fidelity over broad C-rate ranges.

Literature Review. Research on LiB dynamic modeling has flourished in the past decades to produce an extensive collection of literature. The mainstream models generally fall into two categories: electrochemical models and equivalent circuit models (ECMs). Electrochemical models explicitly describe electrochemical reactions, transport of lithium ions, and distribution of charge and potential inside a LiB

cell. Depending on the need for accuracy, they exist on diverse scales, from atomic/molecular to species level, and in different dimensions, from 1D to 3D and beyond, and are often coupled with different physical processes, e.g., thermodynamics and stress/strain [4]. Generally, electrochemical models present high mechanistic fidelity as well as high computational complexity. Battery management researchers hence must selectively focus on those that offer a desirable accuracy–computation trade-off, due to practical demands for fast computation. A favorable choice is the pseudo-2D Doyle–Fuller–Newman (DFN) model, which describes the diffusion of lithium ions and charge transfer across the electrodes, electrolyte, and separator of a sandwich cell [5]. The search for more efficient models has led to the single-particle model (SPM), which represents each electrode by a single spherical particle and neglects electrolyte dynamics [6]. The simplification enhances computational efficiency to a great extent but also limits the SPM model to low-to-moderate C-rates (around or less than 1 C). Subsequent studies have emerged to expand the SPM model by adding characterization of a cell's thermal behavior [7,8], electrolyte dynamics [9–13], stress buildup [13], or degradation [14], to elevate its prediction capability. The literature has also presented a few computational methods to speed up the simulation of the SPM model or its improved versions [15,16].

* Corresponding author.

E-mail address: fang@ku.edu (H. Fang).

ECMs represent another important pathway to modeling LiBs. They are circuit analogs composed of electrical components to simulate a cell's dynamic behavior, capture phenomena in charging/discharging, and track state-of-charge (SoC) and power capability. With simple structures, they are accessible for interpretation, easy to calibrate, and scalable to large LiB systems composed of many cells. Also, they are governed by low-order ordinary differential equations, which allows for very fast computation. These benefits combine to make them popular candidates for real-world battery management systems with limited computing resources [17]. A basic ECM, called the Rint model, cascades an open-circuit voltage (OCV) source with an internal resistor, in which the voltage source is SoC-dependent [18]. The Rint model can be added to a set of serially connected RC pairs to describe the transient behavior in a cell's voltage response, leading to the so-called Thevenin model [1, 19]. Depending on the number of RC pairs used, one can set the model to capture transients at multiple time scales [20]. The literature has presented a few approaches to modify the Thevenin model for better accuracy. For example, the study in [3,21] incorporates hysteresis in charging/discharging; in [22–25], different circuit parameters (e.g., the internal resistance) are made dependent on the SoC, temperature, or current loads, and the OCV is parameterized using different function forms for higher fitting accuracy. Even though phenomenological ECMs and electrochemical models were largely two disparate threads of research, a growing number of studies have explored developing ECMs drawing upon electrochemical modeling. The work in [26,27] proposes the nonlinear double capacitor (NDC) model to approximate the ion diffusion in the electrodes of a cell and characterize the nonlinear voltage behavior simultaneously. This model is interpretable as a reduced-order circuit analog to the SPM, and it is further supplemented in [28] with a data-based voltage hysteresis model to attain better accuracy. The study in [29] derives an ECM using circuit elements to characterize charge transfer and diffusion potentials; the derivation also helps explain some conventional ECMs from an electrochemical perspective. In [30], an ECM is coupled with diffusion dynamics to attain higher prediction accuracy. It is increasingly recognized that we can combine ECMs with machine learning. Such hybrid models, by design, utilize data-driven representation to elevate the accuracy of ECMs in presence of biases or uncertainty, as reported in [31–33].

Structural simplicity underlies the wide use of ECMs in battery management but also restricts their accuracy. Most of today's ECMs are accurate enough for only low C-rates, and recent progress has led to ECMs that are provably suitable for about 1 C [26,27]. However, the literature still faces an absence of ECMs capable of predicting a cell's voltage behavior from low to high C-rate ranges. This gap will pose potential barriers for some emerging battery-powered applications that must operate across wide current ranges. One example is electric vertical take-off and landing (eVTOL), which requires discharging of up to 5 C in the take-off and landing phases and necessitates precise models to fulfill high-stakes safety requirements [34].

Statement of Contributions. In this study, we present the first ECM designed to predict over broad current ranges. We take inspirations from the SPM with electrolyte and thermal dynamics (SPMeT) to enable the design. Specifically, we propose equivalent circuits to separately simulate a LiB cell's electrode, electrolyte, and thermal dynamics as well as their effects on the terminal voltage, and then conjoin the circuits to set up the ECM. The obtained model, called BattX, comprehensively accounts for different dynamic processes key to a cell's charging/discharging behavior, making it distinct from existing ECMs. This characteristic endows the model with excellent prediction capability from low to high C-rates. The model also retains relatively compact structures to offer high computational efficiency, carrying the potential to facilitate embedded battery management applications. Centering around the BattX model, this paper delivers the following specific contributions.

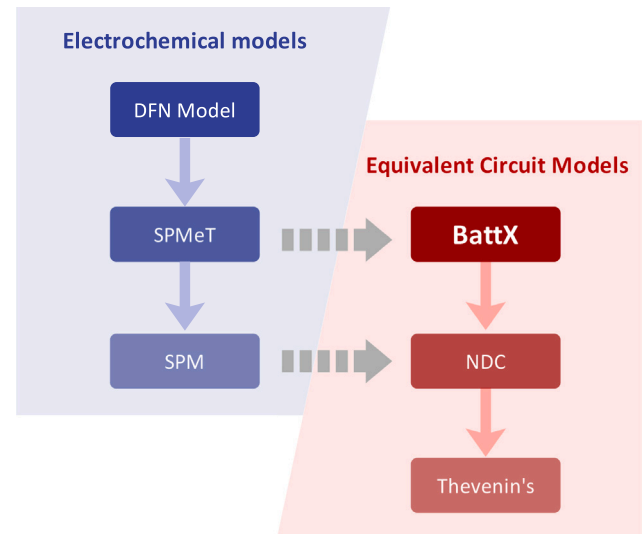


Fig. 1. Relations of the BattX model with some existing battery models. The light blue and red arrows represent model simplification; the gray dashed arrows represent comparability.

- We propose the principled design of the BattX model and further elucidate the underlying rationale by showing its connections with the SPMeT model in detail.
- We develop a multipronged parameter identification approach to extract the parameters of the BattX model from measurement data made on LiBs. This approach can make the model readily available in practice.
- We provide experimental evaluation results to validate the effectiveness and accuracy of the BattX model. The experiments involve charging/discharging across broad C-rate ranges and consider operation profiles of eVTOL as a case study.

Fig. 1 further illustrates the connections of the BattX model with some existing models. As is shown, there is a cascade of simplification from the DFN to the SPMeT to the SPM model in the domain of electrochemical models, and the simplification goes from the BattX to the NDC to the Thevenin model in the domain of ECMs. The BattX model is an ECM in form but can be viewed as a circuit analog to the SPMeT model. It thus combines the respective advantages of both types of models to be fast and accurate. Note that the SPMeT model allows for mathematical model order reduction to speed up computation. However, compared to those numerical reduced-order models, the BattX model well lends itself to physical interpretability and experimental calibration.

Organization. The rest of the paper is organized as follows. Section 2 presents the BattX model design as a whole. Section 3 proceeds to elucidate the model's correspondence to the SPMeT model. Section 4 develops the parameter identification pipeline of the model. Section 5 evaluates the model using experimental data. Finally, Section 6 offers concluding remarks.

2. The BattX model

This section presents the structure and governing equations of the BattX model. We will provide the detailed rationale for the model design subsequently in Section 3.

At the core, the BattX model attempts to characterize the multiple major dynamic processes innate to a LiB cell in order to capture the cell's behavior from low to high current rates. This is akin to electrochemical modeling to a certain extent, but the main difference is that the BattX model leverages circuit analogs to simulate the processes. Fig. 2 shows the overarching structure of the model. As is seen, it

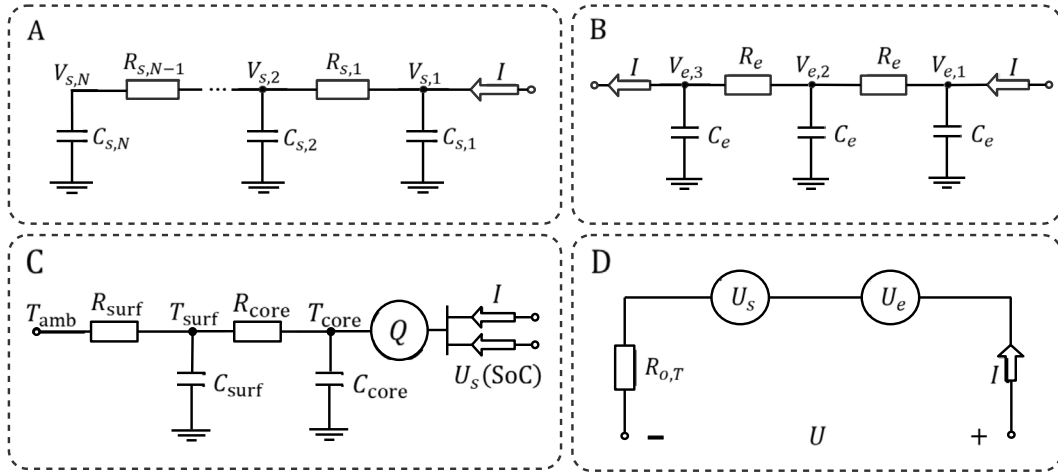


Fig. 2. The BattX model comprising: sub-circuit A to simulate the lithium-ion diffusion in the electrode phase; sub-circuit B to simulate the lithium-ion diffusion in the electrolyte phase; sub-circuit C to simulate heat conduction and convection; and sub-circuit D to simulate the terminal voltage.

consists of four coupled sub-circuits, which are labeled A to D. These sub-circuits are designed to approximate the cell's electrode-phase diffusion, electrolyte-phase diffusion, thermal evolution, and voltage response, respectively.

To begin with, sub-circuit A uses a chain of resistors and capacitors to approximate the lithium-ion diffusion in the electrode phase. Its governing equations are

$$\dot{V}_{s,1}(t) = \frac{V_{s,2}(t) - V_{s,1}(t)}{C_{s,1}R_{s,1}} + \frac{I(t)}{C_{s,1}}, \quad (1a)$$

$$\dot{V}_{s,i}(t) = \frac{V_{s,i-1}(t) - V_{s,i}(t)}{C_{s,i}R_{s,i-1}} + \frac{V_{s,i+1}(t) - V_{s,i}(t)}{C_{s,i}R_{s,i}}, \quad i = 2, \dots, N-1 \quad (1b)$$

$$\dot{V}_{s,N}(t) = \frac{V_{s,N-1}(t) - V_{s,N}(t)}{C_{s,N}R_{s,N-1}}, \quad (1c)$$

where I is the applied current, with $I > 0$ for charging and $I < 0$ for discharging, $V_{s,j}$ for $j = 1, \dots, N$ are the voltages across the individual capacitors $C_{s,j}$, $R_{s,j}$ are the resistors that the current must flow through, and the subscript s refers to the solid phase. We set $0 \leq V_{s,j} \leq 1$ for the purpose of normalization and then define the SoC as the percentage ratio of the currently available charge over the total charge capacity, which is

$$\text{SoC} = \frac{\sum_{j=1}^N C_{s,j} V_{s,j}}{\sum_{j=1}^N C_{s,j}} \times 100\%.$$

That is, SoC = 100% when $V_{s,j} = 1$ for all j , and SoC = 0 when $V_{s,j} = 0$ for all j . A brief interpretation of sub-circuit A is as follows, with more details to be shown in Section 3. Overall, the charge transfer between the capacitors in the circuit mimics the diffusion of lithium ions in the solid phase or electrode. Then, $V_{s,j}$ for $j = 1, \dots, N$ correspond to the lithium-ion concentrations at N different locations, from the surface to the center, that spread along the radius of an electrode sphere; $C_{s,j}$ for $j = 1, \dots, N$ are analogous to the volumes of the subdomains if one subdivides the electrode sphere at these discrete locations; $R_{s,j}$ for $j = 1, \dots, N-1$ resist the charge transfer or equivalently, the solid-phase diffusion in the SPMET model, and are hence inversely proportional to the diffusivity.

Along similar lines to sub-circuit A, sub-circuit B uses a resistor-capacitor chain to approximate the lithium-ion diffusion in the electrolyte. Its dynamics are governed by

$$\dot{V}_{e,1}(t) = \frac{V_{e,2}(t) - V_{e,1}(t)}{C_e R_e} + \frac{I(t)}{C_e}, \quad (2a)$$

$$\dot{V}_{e,2}(t) = \frac{V_{e,1}(t) - 2V_{e,2}(t) + V_{e,3}(t)}{C_e R_e}, \quad (2b)$$

$$\dot{V}_{e,3}(t) = \frac{V_{e,2}(t) - V_{e,3}(t)}{C_e R_e} - \frac{I(t)}{C_e}, \quad (2c)$$

where the notations in above have similar meanings as in (1), and the subscript e refers to the electrolyte. We let $0 \leq V_{e,j} \leq 1$ for $j = 1, 2, 3$ as in the case of $V_{s,j}$, and further assume that $V_{e,j} = 0.5$ for $j = 1, 2, 3$ when the cell is at equilibrium. One can interpret sub-circuit B as analogous to the one-dimensional electrolyte-phase diffusion that is discretized along the spatial coordinate. In particular, $V_{e,j}$ for $j = 1, 2, 3$ can be associated with the lithium-ion concentrations at the locations of the anode, separator, and cathode, and R_e embodies resistance to the diffusion. The spatial discretization is assumed to be uniform, thus leading to the same values of R_e and C_e for each region as shown in (2).

Sub-circuit C is a lumped circuit model for the thermal dynamics, with the design inspired by [35]. Here, we consider the cell to be a cylindrical one without loss of generality and concentrate its spatial dimensions into two singular points that represent the surface and core, respectively. This simplification allows us to describe the evolution of the temperatures at these two points, T_{surf} and T_{core} , by

$$\dot{T}_{\text{core}}(t) = \frac{Q(t)}{C_{\text{core}}} + \frac{T_{\text{surf}}(t) - T_{\text{core}}(t)}{R_{\text{core}} C_{\text{core}}}, \quad (3a)$$

$$\dot{T}_{\text{surf}}(t) = \frac{T_{\text{amb}}(t) - T_{\text{surf}}(t)}{R_{\text{surf}} C_{\text{surf}}} - \frac{T_{\text{surf}}(t) - T_{\text{core}}(t)}{R_{\text{core}} C_{\text{surf}}}, \quad (3b)$$

where T_{amb} is the ambient temperature, $C_{\text{surf/core}}$ and $R_{\text{surf/core}}$ represent the thermal capacitance and resistance at the surface and core, respectively, and Q is the internal heat generation rate accompanying electrochemical reactions inside the cell during charging/discharging. From a heat transfer perspective, (3a) approximately describes the heat conduction between the cell's surface and core, and (3b) grasps the convection between the surface and the ambient environment. Further, Q is characterized as

$$Q = -I [U_s(\text{SOC}) - U_s(V_{s,1}) - R_{o,T} I], \quad (4)$$

where $U_s(\cdot)$ is the nonlinear OCV function, $V_{s,1}$ is defined in sub-circuit A, and $R_{o,T}$ is the internal resistance.

Finally, sub-circuit D summarizes the effects of the solid-phase and electrolyte-phase dynamics on the terminal voltage. It contains two voltage sources, U_s and U_e , in series with an internal resistance $R_{o,T}$. The terminal U is given by

$$U = U_s(V_{s,1}(t)) + U_e(V_{e,1}(t), V_{e,N_e}(t)) + R_{o,T} I(t). \quad (5)$$

Here, U_s simulates the solid-phase OCV. As the SPMET model mandates that the open-circuit potential of solid material relies on the lithium-ion concentration at the surface of the electrode, U_s should come as a function of $V_{s,1}$, and its exact form will depend on the cell. Next, we

need to determine the form of U_e . In the SPMeT model, the electrolyte potential depends on the electrolyte concentration at the anode and cathode. We hence make U_e as a function of $V_{e,1}$ and V_{e,N_e} and express it as

$$U_e(t) = \beta_1 \left(\ln \left(\frac{V_{e,1}(t) + \beta_2}{V_{e,3}(t) + \beta_2} \right) \right), \quad (6)$$

where β_i for $i = 1, 2$ are constant coefficients. As the last element of the model, $R_{o,T}$ is not a constant and instead depends on SoC and T_{core} . It is given by

$$R_{o,T} = R_o(\text{SoC}) \cdot \exp \left(\kappa_1 \left(\frac{1}{T_{core}} - \frac{1}{T_{amb}} \right) \right), \quad (7)$$

where κ_1 is a constant coefficient. In above, the first term $R_o(\text{SoC})$ captures the dependence of $R_{o,T}$ on $V_{s,1}$ and takes the form

$$R_o(\text{SoC}) = \gamma_1 + \gamma_2 \cdot \exp(-\gamma_3 \text{SoC}), \quad (8)$$

where γ_i for $i = 1, 2, 3$ are coefficients, and the second term shows the temperature dependence due to the Arrhenius law. Similarly, an Arrhenius relationship can be used to capture the relationship between the electrode-phase diffusion constant and temperature:

$$R_{s,1,T} = R_{s,1} \cdot \exp \left(\kappa_2 \left(\frac{1}{T_{core}} - \frac{1}{T_{amb}} \right) \right). \quad (9)$$

Putting together all the above equations, we will obtain a complete description of the BattX model. This model is the first ECM that can predict over broad current ranges, due to the integration of the circuits approximating the electrode, electrolyte, and thermal dynamics into a whole. The model design also leads to profound comparability with electrochemical modeling, especially the SPMeT, which will be revealed further in the next section. We will address the identification of the model parameters in Section 4.

3. Rationale for the BattX model design

In this section, we will draw on the SPMeT model to explain the rationale for the design of the BattX model. We will show that the SPMeT model if appropriately discretized, will reduce to a structure that is approximately equivalent to the proposed circuit analogs of the BattX model. Our main references about the SPMeT model include [12, 36,37]. We will focus on expounding sub-circuits A, B, and D, with the sub-circuit C-based lumped thermal model well addressed in [35].

3.1. Connection between sub-circuit A and SPMeT

The SPMeT model characteristically couples the SPM model with the electrolyte and thermal dynamics. What it inherits from the SPM model is the representation of the electrodes as two spherical particles. The diffusion of lithium-ions in each particle follows Fick's second law in spherical coordinates [7,8]:

$$\frac{\partial c_{s,j}(r,t)}{\partial t} = \frac{D_{s,j}}{r^2} \frac{\partial}{\partial r} \left(r^2 \frac{\partial c_{s,j}(r,t)}{\partial r} \right), \quad (10)$$

where $c_{s,j}$ is the solid-phase (electrode) lithium-ion concentration, D_s is the constant diffusion coefficient, and r is the radial coordinate. The subscript $j \in \{n, p\}$, where n and p refer to the anode (negative) and cathode (positive), respectively. The boundary conditions for (10) are

$$\left. \frac{dc_{s,j}}{dr} \right|_{r=0} = 0, \quad \left. \frac{dc_{s,j}}{dr} \right|_{r=R_j} = -\frac{J_j}{D_{s,j}},$$

where R is the radius of a particle. The molar flux J at the electrode/electrolyte interface is given by

$$J_p(t) = \frac{i(t)}{FS_p}, \quad J_n(t) = -\frac{i(t)}{FS_n},$$

where i is the applied current density, with $i > 0$ for charging and $i < 0$ for discharging, S is the surface area of a particle, and F is Faraday's constant.

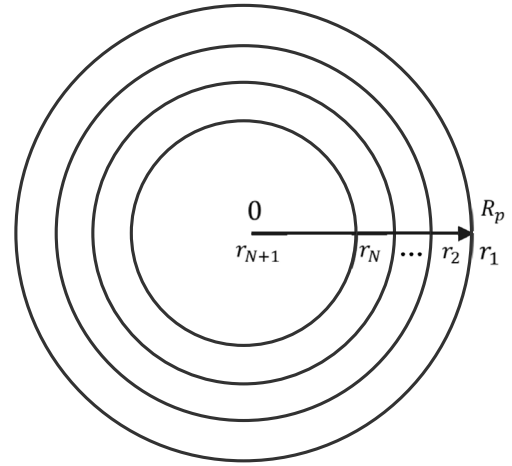


Fig. 3. Spherical discretization of an electrode particle.

Next, let us reduce the PDE in (10) into a system of ODE equations using a finite volume method [38,39]. The subscript $j \in n, p$ will be dropped in sequel without causing confusion. First, we subdivide the particle into a set of continuous finite volumes at discrete locations $r_1 = R > r_2 > \dots > r_N > r_{N+1} = 0$ that spreads inward from the surface to the center, as show in Fig. 3. The amount of lithium-ions within the i th finite volume is given by

$$Q_i(t) = \int_{r_{i+1}}^{r_i} c_s(r,t) dV = \int_{r_{i+1}}^{r_i} c_s(r,t) \cdot 4\pi r^2 dr,$$

for $i = 1, \dots, N$. Then, using (10), we have

$$\begin{aligned} \dot{Q}_i(t) &= \int_{r_{i+1}}^{r_i} \dot{c}_s(r,t) \cdot 4\pi r^2 dr = \int_{r_{i+1}}^{r_i} d \left(4\pi D_s r^2 \frac{\partial c_s(r,t)}{\partial r} \right) \\ &= 4\pi D_s r_i^2 \left. \frac{\partial c_s(r,t)}{\partial r} \right|_{r_i} - 4\pi D_s r_{i+1}^2 \left. \frac{\partial c_s(r,t)}{\partial r} \right|_{r_{i+1}}. \end{aligned} \quad (11)$$

To proceed, we replace $c_s(r,t)$ by the average lithium-ion concentration within the i th finite volume, $\bar{c}_s(r_i,t)$:

$$\bar{c}_s(r_i,t) = \frac{Q_i(t)}{\Delta V_i}, \quad (12)$$

where $\Delta V_i = 4\pi(r_i^3 - r_{i+1}^3)/3$. From (11)–(12), it follows that

$$\dot{\bar{c}}_s(r_i,t) = \frac{4\pi D_s r_i^2}{\Delta V_i} \left. \frac{\partial c_s(r,t)}{\partial r} \right|_{r_i} - \frac{4\pi D_s r_{i+1}^2}{\Delta V_i} \left. \frac{\partial c_s(r,t)}{\partial r} \right|_{r_{i+1}}.$$

Then, we approximate the concentration gradient along the radial coordinate as

$$\left. \frac{\partial c_s(r,t)}{\partial r} \right|_{r_i} = \frac{\bar{c}_s(r_{i-1},t) - \bar{c}_s(r_i,t)}{\Delta r_i},$$

where $\Delta r_i = (r_{i-1} - r_{i+1})/2$. Given the boundary conditions, we further have

$$\dot{\bar{c}}_s(r_1,t) = -\frac{4\pi D_s r_1^2}{\Delta V_1 \Delta r_2} (\bar{c}_s(r_1,t) - \bar{c}_s(r_2,t)) + \frac{4\pi r_1^2}{\Delta V_1 F S} i(t), \quad (13a)$$

$$\begin{aligned} \dot{\bar{c}}_s(r_i,t) &= \frac{4\pi D_s r_i^2}{\Delta V_i \Delta r_i} (\bar{c}_s(r_{i-1},t) - \bar{c}_s(r_i,t)) \\ &\quad - \frac{4\pi D_s r_{i+1}^2}{\Delta V_i \Delta r_{i+1}} (\bar{c}_s(r_i,t) - \bar{c}_s(r_{i+1},t)), \quad i = 2, \dots, N-1, \end{aligned} \quad (13b)$$

$$\dot{\bar{c}}_s(r_N,t) = \frac{4\pi D_s r_N^2}{\Delta V_N \Delta r_N} (\bar{c}_s(r_{N-1},t) - \bar{c}_s(r_N,t)). \quad (13c)$$

The above ODEs show the spatially discretized solid-phase diffusion. Note that they share the same structure with (1). A closer inspection of (1) and (13) suggests: (1) V_s is a mirror of $\bar{c}_s(r,t)$, and its distribution reflects the distribution of lithium-ion concentrations inside an

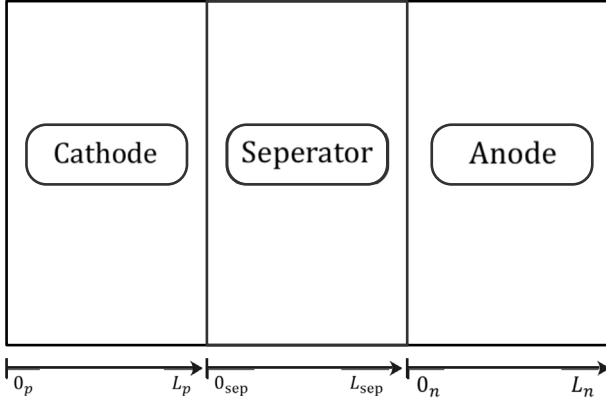


Fig. 4. Three regions immersed in the electrolyte.

electrode particle; (2) C_s is a mirror of ΔV , associating the capacitance with the volume of a finite volume element within the particle; (3) R_s roughly corresponds to $\Delta r / (D_s \cdot 4\pi r^2)$ to grasp the effect of D_s , Δr and r on the diffusion resistance at different locations. This unveiled connection with the SPMeT model justifies the design of sub-circuit A.

3.2. Connection between sub-circuit B and SPMeT

The SPMeT model includes one-dimensional electrolyte diffusion, which also follows Fick's second law. Electrolyte diffusion is considered in the electrode and separator domains that are all immersed in the electrolyte. Based on the coordinates in each domain as shown in Fig. 4, the governing equations are

$$\frac{\partial c_{e,p}(x,t)}{\partial t} = D_e \frac{\partial^2 c_{e,p}(x,t)}{\partial x^2} + \frac{1-t_c^0}{\epsilon_{e,p} F L_p} i(t), \quad (14a)$$

$$\frac{\partial c_{e,sep}(x,t)}{\partial t} = D_e \frac{\partial^2 c_{e,sep}(x,t)}{\partial x^2}, \quad (14b)$$

$$\frac{\partial c_{e,n}(x,t)}{\partial t} = D_e \frac{\partial^2 c_{e,n}(x,t)}{\partial x^2} - \frac{1-t_c^0}{\epsilon_{e,n} F L_n} i(t), \quad (14c)$$

where $c_{e,j}$ for $j \in \{n, p, sep\}$ is the lithium-ion concentration in the electrolyte surrounding the anode, cathode and separator, $\epsilon_{e,j}$ is the electrolyte volume fraction, $D_{e,j}$ is the electrolyte diffusion coefficient, and t_c^0 is the constant transference number. We assume that $\epsilon_{e,j}$ and $D_{e,j}$ are the same for any $j \in \{n, p, sep\}$. The boundary conditions are given by

$$\begin{aligned} \frac{\partial c_{e,p}(0_p,t)}{\partial x} &= \frac{\partial c_{e,n}(L_n,t)}{\partial x} = 0, \\ \frac{\partial c_{e,p}(L_p,t)}{\partial x} &= \frac{\partial c_{e,sep}(0_{sep},t)}{\partial x}, \\ \frac{\partial c_{e,sep}(L_{sep},t)}{\partial x} &= \frac{\partial c_{e,n}(0_n,t)}{\partial x}, \\ c_e(L_p,t) &= c_e(0_{sep},t), \\ c_e(L_{sep},t) &= c_e(L_n,t). \end{aligned}$$

To convert (14) into ODEs, we concentrate the electrodes and separator into singular points and further suppose $L_p = L_n$ and L_{sep} is negligible. The singular point that represents the electrodes are located at the midpoint of each domain, and the average lithium-ion concentration is denoted as $\bar{c}_{e,j}$. Then, we apply the finite difference method to (14) and obtain

$$\dot{\bar{c}}_{e,p}(t) = \frac{4D_e}{L^2} (\bar{c}_{e,sep}(t) - \bar{c}_{e,p}(t)) + \frac{1-t_c^0}{\epsilon_e F L} i(t), \quad (15a)$$

$$\dot{\bar{c}}_{e,sep}(t) = \frac{4D_e}{L^2} (\bar{c}_{e,p}(t) - 2\bar{c}_{e,sep}(t) + \bar{c}_{e,n}(t)), \quad (15b)$$

$$\dot{\bar{c}}_{e,n}(t) = \frac{4D_e}{L^2} (\bar{c}_{e,sep}(t) - \bar{c}_{e,n}(t)) - \frac{1-t_c^0}{\epsilon_e F L} i(t). \quad (15c)$$

As is seen, (14) is structurally similar to (2), and the similarity lends to the interpretation of (2) through the lens of electrochemical modeling. Specifically, we can associate $V_{e,1}$, $V_{e,2}$ and $V_{e,3}$ with $\bar{c}_{e,p}$, $\bar{c}_{e,sep}$, and $\bar{c}_{e,n}$, respectively. Further, C_e can be linked with the spatial lengths of the electrode domains, which decide the volume of the electrolyte, and R_e comes as the inverse of D_e to measure the resistance against electrolyte diffusion.

3.3. Connection between sub-circuit D and SPMeT

In the SPMeT model, the terminal voltage V consists of four terms that represent the solid-phase OCV, electrolyte-phase voltage, overpotential, and voltage over the film resistance, respectively. Then, coming back to sub-circuit D of the BattX model, U_s mirrors the solid-phase OCV, U_e corresponds to the electrolyte-phase voltage, and $R_{o,T}$ plays a role to mainly capture the film resistance as well as the overpotential effect. Less trivially, we elaborate on the form of U_e in (6). The electrolyte-phase voltage is given by

$$\phi_e(0_p,t) - \phi_e(L_n,t) = \frac{L_p + 2L_{sep} + L_n}{2\bar{k}} i(t) + k_{conc} (\ln c_e(0_p,t) - \ln c_e(L_n,t)), \quad (16)$$

where ϕ_e is the electrolyte electric potential, and \bar{k} and k_{conc} are two coefficients that are related to electrolyte conductivity and molar activity. The first term above is accounted for through $R_{o,T}$. Following the discussion in Section 3.2, we can approximate the second term as

$$k_{conc} (\ln \bar{c}_{e,p}(t) - \ln \bar{c}_{e,n}(t)).$$

This form is found to bear equivalence to (6), when making linear projections of $\bar{c}_{e,p}(t)$ and $\bar{c}_{e,n}(t)$ to $V_{e,1}$ and $V_{e,3}$, respectively.

4. Parameter identification for the BattX model

In this section, we investigate how to determine the parameters of the BattX model. To this end, we separate the model's parameters into different groups based on the dynamic processes that they belong to or prominently influence. We then design experiments accordingly and use different current profiles to excite different dynamic processes and obtain voltage or temperature data suitable for the identification of the corresponding parameter groups. Finally, we extract the parameters from the data, group by group, through data fitting and some empirical tuning.

To begin with, we set up the following parameter groups for the BattX model:

- $\Theta_{U_s} = \{a_i, i = 0, 1, \dots, 16\}$, which includes the parameters in U_s in sub-circuit D;
- $\Theta_{R_o} = \{\gamma_i, i = 1, 2, 3\}$, which includes the parameters in R_o in sub-circuit D;
- $\Theta_s = \{C_{s,i}, i = 1, \dots, N, R_{s,j}, j = 1, \dots, N-1\}$, which includes the parameters of sub-circuit A;
- $\Theta_{Th} = \{C_{surf}, R_{surf}, C_{core}, R_{core}\}$, which includes the parameters in the lumped thermal model in sub-circuit C;
- $\Theta_e = \{C_e, R_e, \beta_1, \beta_2\}$, which includes the parameters in sub-circuit B and the parameters in U_e in sub-circuit D;
- $\Theta_{Arr} = \{\kappa_1, \kappa_2\}$, which includes the Arrhenius-law-related parameters;

By grouping the parameters as above, we can design different current input profiles to stimulate different parts of the cell's dynamics so as to identify the parameters group by group. This multi-pronged approach includes the following steps.

Step 1: Identification of Θ_{U_s} . Since U_s represents the OCV source, we can capture it by applying a trickle constant current with a magnitude of 1/30 C to fully charge or discharge the cell. As the current is extremely small, sub-circuit A, which is an analog to the solid (electrode)-phase diffusion, is almost always at equilibrium, with $V_{s_i} = \text{SoC}$ for $i = 1, \dots, N$ (SoC can be obtained via Coulomb counting); meanwhile, sub-circuits B and C, U_e , and the voltage across $R_{o,T}$, are all negligible in this case. Hence, $U \approx U_s$, and we can construct the following data fitting problem to identify Θ_{U_s} :

$$\hat{\Theta}_{U_s} = \arg \min_{\Theta_{U_s}} \sum_{t_k} \left[U(t_k) - U_s(\text{SoC}(t_k); \Theta_{U_s}) \right]^2, \quad (17)$$

where k is the discrete time index in the experiment.

Step 2: Identification of Θ_{R_o} . R_o is an integral part of the internal resistance $R_{o,T}$, and $R_o = R_{o,T}$ when $T = T_{\text{ref}}$. To identify Θ_{R_o} , we apply a 0.5 C pulse current profile, which includes long enough rest periods between two consecutive pulses to allow for sufficient voltage recovery, to discharge the cell from 100% to 0% of SoC when the ambient temperature is T_{ref} . With discharging at 0.5 C, the cell will only see a negligible increase in its temperature, and $U_e \approx 0$. For the terminal voltage U , we will see a sharp drop or jump at the beginning or end of every pulse, and this is almost solely due to the voltage change across R_o . Therefore, using the voltage jump, one can approximate R_o as

$$\hat{R}_o(t_*) = \left| \frac{U(t_{*+1}) - U(t_*)}{I} \right|, \quad (18)$$

where t_* is the instant when a pulse stops. Further, the instantaneous SoC can be readily determined via Coulomb counting. Collecting R_o for all t_* , we can formulate the following data fitting problem to estimate Θ_{R_o} :

$$\hat{\Theta}_{R_o} = \arg \min_{\Theta_{R_o}} \sum_{t_*} \left[\hat{R}_o(t_*) - R_o(\Theta_{R_o}; t_*) \right]^2. \quad (19)$$

Step 3: Identification of Θ_s . The number of parameters in Θ_s depends on N , and when N is large, Θ_s will be poorly identifiable to defy accurate estimation. To formulate a tractable identification problem, we assume that

$$C_{s,i} = \eta_i C_{s,1}, \quad R_{s,j} = \sigma_j R_{s,1}, \quad (20)$$

where η_i and σ_j for $i = 1, \dots, N$ and $j = 1, \dots, N - 1$ are pre-specified coefficients with $\eta_1 = \sigma_1 = 1$, and $\sum_{i=1}^N \eta_i C_{s,i}$ is the total capacity of the cell. This allows us to consider only two parameters, i.e., $\Theta_s = \{C_{s,1}, R_{s,1}\}$, greatly facilitating the parameter estimation. The simplification is also reasonable—the difference among $C_{s,i}$ and $R_{s,j}$ can be viewed as a result of the selection of the discretization points as shown in (13), and one can specify η_i and σ_j assuming that they result from a certain selection. The practical selection of η_i and σ_j can be done through an analysis of the discretization shown in Section 3.1 and tuning. Going forward, we apply a 0.5 C constant-current profile to discharge the cell from full to zero SoC. In this setting, sub-circuit A is excited, but the dynamics of sub-circuits B and C have no appreciable effects. That is, the cell's temperature remains almost the same, and $U_e \approx 0$. We can conduct data fitting as below to find out Θ_s :

$$\hat{\Theta}_s = \arg \min_{\Theta_s} \sum_{t_k} \left[U(t_k) - R_o(\hat{\Theta}_{R_o}; t_k) I(t_k) - U_s(V_{s,1}(\Theta_s; t_k); \hat{\Theta}_{U_s}) \right]^2, \quad (21)$$

where $\hat{\Theta}_{U_s}$ and $\hat{\Theta}_{R_o}$ have been obtained in Steps 1 and 2, and the form of $V_{s,1}(\Theta_s, t)$ is derived in Appendix A.

Step 4: Identification of Θ_{Th} . Based on [35], a straightforward idea to determine Θ_{Th} is to fit it to the measurement data of T_{surf} and/or T_{core} given the lumped thermal model in (3). However, the idea is hard to be applied here, because Q in our model is dependent on $R_{o,T}$, as shown in (4), and unavailable before $R_{o,T}$ is identified. To overcome

this issue, we choose to use prior knowledge to guide the estimation of Θ_{Th} . Here, we can approximate R_{core} based on the conductivity of the cell's electrode materials and jellyroll structure. Furthermore, we can infer R_{surf} and C_{surf} from the form factors and specifications, casing material (usually aluminum), and the cooling system. Finally, C_{core} can be deduced given the cell's total heat capacity. A 2C constant current full discharge profile is used to acquire the data encompassing significant temperature changes. With the measurement data, we can begin from the approximate values of the parameters and continually tune them until achieving sufficient fitting accuracy to finalize Θ_{Th} .

Step 5: Identification of Θ_e and Θ_{Arr} . Sub-circuit B will have substantial effects on U only at high C-rates. Therefore, we use a 3 C constant current profile to fully discharge the cell such that large enough U_e will result and present itself into the voltage response. This then allows to identify Θ_e . In the meantime, 3 C discharging will subject the cell to important temperature increases, which, in turn, will drive down Θ_{Arr} -dependent $R_{s,T}$ and $R_{o,T}$ and influence the voltage response. As such, we need to consider the estimation of Θ_e and Θ_{Arr} together. The following data fitting problem can be formulated:

$$\hat{\Theta}_e, \hat{\Theta}_{\text{Arr}} = \arg \min_{\Theta_e, \Theta_{\text{Arr}}} \sum_{t_k} \left[U(t_k) - R_{o,T}(\hat{\Theta}_{R_o}, \Theta_{\text{Arr}}, T_k; t_k) I(t_k) - U_s(V_{s,1}(\hat{\Theta}_s, \Theta_{\text{Arr}}, T_k; t_k); \hat{\Theta}_{U_s}) - U_e(\Theta_e; t_k) \right]^2. \quad (22)$$

Here, U_e depends on $V_{e,1}$ and $V_{e,3}$ as shown in (6), and the explicit form of $V_{e,1}$ and $V_{e,3}$ is shown in Appendix B. Note that no closed-form expression of U_s exists in this step, as the changing $R_{s,T}$ makes sub-circuit A become a time-varying system. It is thus impossible to solve the problem in (22) using nonlinear optimization. To alleviate the difficulty, we suggest to apply some empirical tuning. Specifically, we can pick a sample of Θ_{Arr} using prior knowledge, then estimate Θ_e by solving the above data fitting problem, and iterate this procedure until getting the lowest possible fitting errors. Despite the time and effort needed, this iterative method is often found effective with a sufficient number of tries.

The above steps together constitute our parameter identification approach for the BattX model and are summarized in the flowchart in Fig. 5. The following remarks summarize our further insights.

Remark 1.

We point out that the data fitting problems outlined in Steps 1–5 are non-trivial to solve, as they entail nonlinear nonconvex optimization. The nonconvexity can easily get the parameter search stuck in local minima to produce physically meaningless parameter estimates. To mitigate the issue, it is sensible to constrain the search within a believably correct parameter space [20]. Specifically, one can set up approximate lower and upper bounds for every possible parameter and then limit the numerical optimization within the resultant parameter space. The prior knowledge used to establish such bounds can be derived from both experience and observation or analysis of the measurement data. Other helpful ways to overcome the local minima issue include adding regularization terms that encode prior knowledge of some parameters and applying different initial guesses to repeatedly run the numerical optimization [20].

Remark 2.

We consider Samsung INR18650-25R cells (see Section 5 for the specifications) as a baseline when selecting the discharging C-rates in each step of the above approach, because they are used in the experimental validation of the BattX model (see Section 5). However, a user or practitioner may need to adjust the specific C-rates, depending on the cells to apply the model. The overall guiding rule is the same—using current profiles of different C-rates to excite different dynamic processes to obtain data informative for the identification of the parameters associated with each process.

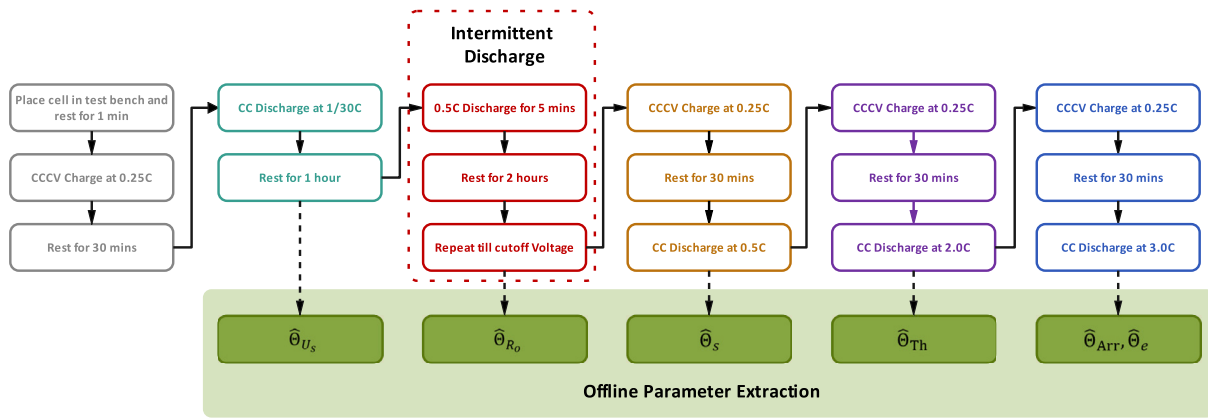
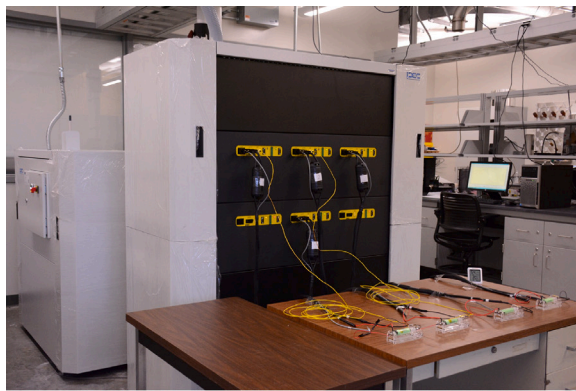
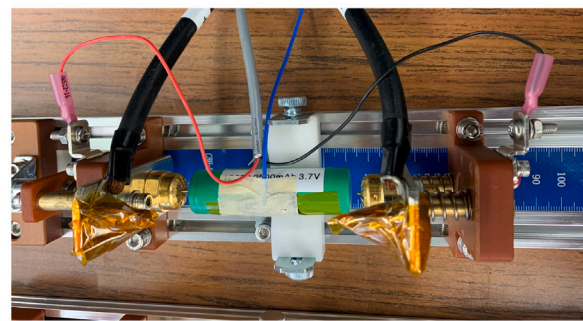


Fig. 5. Flowchart for the multipronged experimental data generation and parameter identification.



(a)



(b)

Fig. 6. Experimental setup: (a) the PEC® SBT4050 battery tester; (b) the cell placed in an Arbin high-current cylindrical cell holder.

Table 1
Identification summary for θ_R , θ_s , and θ_{Th} : initial guesses, bound limits, and final estimates.

Name	γ_1	γ_2	γ_3	$C_{s,1}$	$R_{s,1}$	C_{surf}	R_{surf}	C_{core}	R_{core}
Initial guess	1	1	1	4391	0.090	7	6	20	1
Lower bound	-	-	-	3600	0.054	3	3	5	0.5
Upper bound	-	-	-	5500	0.167	12	20	50	7
Final estimate	0.026	0.061	14.36	4521	0.114	10	7	40	4

5. Experimental validation of the BattX model

This section offers the experimental validation of the proposed BattX model. All the experiments were conducted on a Samsung INR18650-25R cell with NCA cathode and graphite anode using a PEC® SBT4050 battery tester and placed in an Arbin cylindrical cell holder, as shown in Fig. 6. The cell’s nominal capacity is 2.5 Ah, nominal voltage is 3.6 V, maximum cut-off voltage is 4.2 V, minimum cut-off voltage is 2.5 V, and maximum continuous discharge current is 20 A. The tester is able to run charging or discharging tests of up to 40 V and 50 A under arbitrary current or power load profiles. The cell holder is capable of testing high-capacity 18650 cells at up to 200 A.

The experiment is comprised of two parts. The first part collected datasets following the parameter identification approach in Section 4 to identify the model parameters. In the second part, new datasets were generated to evaluate the predictive capability and computational cost of the identified model against the Thevenin model.

5.1. Model identification

The experiments and model identification procedure is as follows.

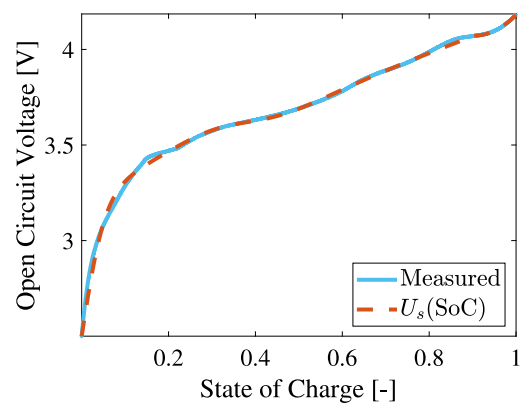


Fig. 7. SoC/OCV curve fitting based on $\hat{\theta}_{U_s}$.

- Based on Section 4, we first charged the cell using the popular constant-current/constant-voltage method, let it rest for one hour, and then fully discharged it using a 1/30 C constant-current load.

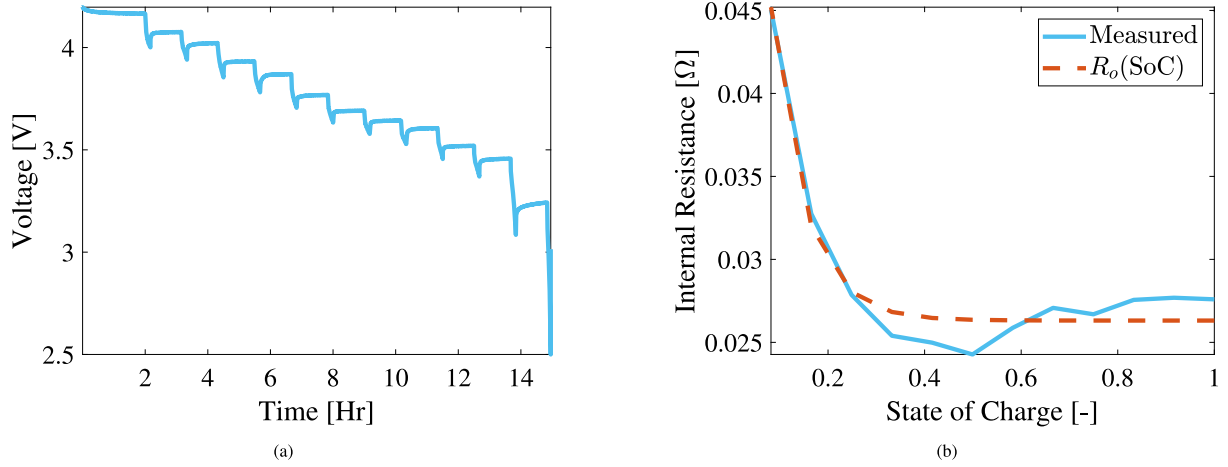


Fig. 8. Identification of θ_{R_o} : (a) terminal voltage profile under intermittent discharging at 0.5 C to identify θ_{R_o} ; (b) fitting of $R_o(\text{SoC})$ with \hat{R}_o based on $\hat{\theta}_{R_o}$.

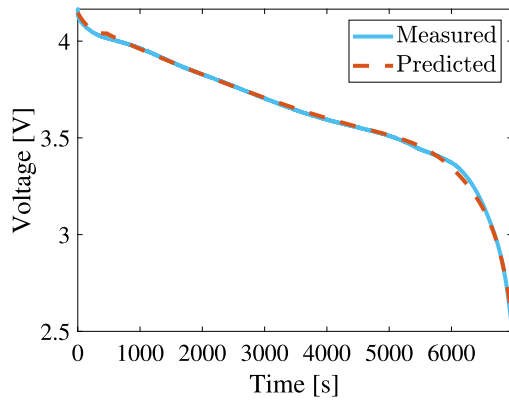


Fig. 9. Terminal voltage fitting under 0.5 C constant-current discharging based on $\hat{\theta}_s$.

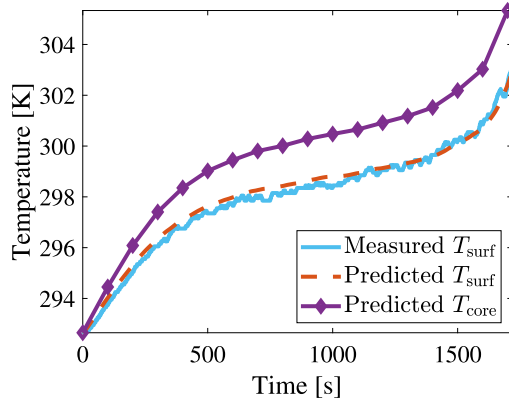


Fig. 10. Temperature fitting and prediction based on $\hat{\theta}_{\text{Th}}$.

We calculated the total capacity to be 2.55 A h using the Coulomb counting method and then intended to use the voltage data to find $\hat{\theta}_{U_s}$. The following non-linear function was used to predict the OCV of the cell:

$$U_s(V_{s,1}) = h_1(V_{s,1}) \cdot H(0.9 - V_{s,1}) + h_2(V_{s,1}) \cdot H(V_{s,1} - 0.9),$$

where $H(\cdot)$ is the Heaviside step function, $h_1(V_{s,1})$ captures the behavior when $V_{s,1} \leq 0.9$ as

$$h_1(V_{s,1}) = \alpha_0 + \alpha_1 \frac{1}{1 + \exp(\alpha_2(V_{s,1}(t) - \alpha_3))}$$

$$+ \alpha_4 \frac{1}{1 + \exp(\alpha_5(V_{s,1} - \alpha_6))} + \alpha_7 \frac{1}{1 + \exp(\alpha_8(V_{s,1} - \alpha_9))} + \alpha_{10} \frac{1}{1 + \exp(\alpha_{11}V_{s,1}(t))} + \alpha_{12}V_{s,1}(t),$$

and $h_2(V_{s,1})$ is for when $0.9 < V_{s,1} \leq 1$ with

$$h_2(V_{s,1}) = \alpha_{13} \exp(\alpha_{14}V_{s,1}) + \alpha_{15} \exp(\alpha_{16}V_{s,1}).$$

Here, α_i for $i = 0, \dots, 15$ are constant coefficients. Then, $\hat{\theta}_{U_s}$ was found based on (17):

$$\hat{\theta}_{U_s} = \{-9.048, -2.360, -12.986, 0.010, 13.036, -32.840, -0.087, 2.359, -14.863, 0.055, -0.788, -7.136, 0.966, 31.132, -3.414, 0.513, 1.816\}.$$

The SoC/OCV fitting result under the obtained $\hat{\theta}_{U_s}$ is shown in Fig. 7.

- Next, the cell was charged to full again, idled for one hour, and then discharged under a 0.5 C pulse load profile. Specifically, a load was applied for five minutes, followed by a one-hour rest, and this cycle continued until the cut-off voltage was met. Fig. 8 shows the profile, which includes a total of 12 pulses. With the data, we calculated R_o at different SoC via (18) and then used (19) to compute $\hat{\theta}_{R_o}$ as shown in Table 1. The reconstructed R_o is compared with the measurements in Fig. 8.
- Going further, we fully charged the cell again as in the previous steps, and then fully discharged it using a 0.5 C constant-current load, with the objective of identifying θ_s . As explained in Section 4, we could impose a pre-determined relation like (20) to reduce the number of parameters to estimate. Here, we let the spherical particle be discretized into five finite volumes, and the resulting η_i and σ_j are

$$\eta_i = \{1, 0.6066, 0.3115, 0.1148, 0.0164\},$$

$$\sigma_j = \{1, 1.77, 4.00, 15.98\}.$$

Fig. 9 illustrates a comparison between the predicted terminal voltage (with the dynamics of sub-circuits B and C neglected) based on $\hat{\theta}_s$ and the measurements. Table 1 shows the estimation for $\hat{\theta}_s$.

- Then, we ran a 2 C constant-current discharging test to collect the temperature data. The cell's surface temperature increased by about 10 K throughout the test. We leveraged prior knowledge and empirical tuning to determine θ_{Th} , as suggested in Section 4. While the procedure is coarse-grained, we obtained $\hat{\theta}_{\text{Th}}$ that leads to accurate fitting with the surface temperature data and physically reasonable estimation of the core temperature, as shown in Fig. 10. Table 1 summarizes the numerical estimates of $\hat{\theta}_{\text{Th}}$.

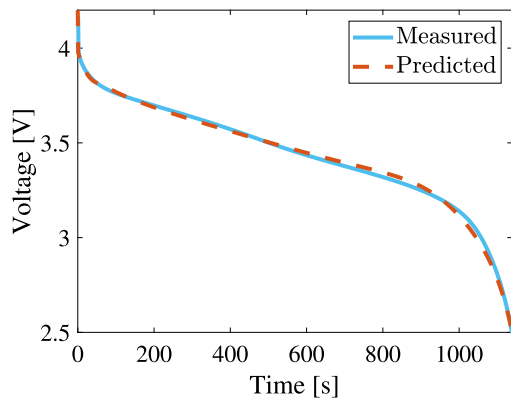


Fig. 11. Terminal voltage fitting under 3 C constant-current discharging based on $\hat{\theta}_e$.

Table 2
Identification summary for θ_{Arr} and θ_e : initial guesses, bound limits, and final estimates.

Name	C_e	R_e	β_1	β_2	κ_1	κ_2
Initial guess	1032	0.028	0.53	0.31	15	22
Lower bound	500	0.002	0.42	0.19	10	10
Upper bound	5000	0.080	1.00	0.423	100	100
Final estimate	3691	0.007	0.789	0.317	30	70

- Finally, the cell was fully discharged at a constant current of 3 C to excite the cell’s electrolyte dynamic and thermal behavior more discernible, for the purpose of identifying θ_e and θ_{Arr} . Following Section 4, we iteratively tuned $\hat{\theta}_{Arr}$ and then ran (22) to find $\hat{\theta}_e$ until the achievement of both physically sound estimates and accurate voltage data fitting. Fig. 11 shows that the BattX model based on all the identified parameters fits well the measured voltage, and Table 2 shows the estimation results.

From above, we have come up with an explicit setup of the BattX model for the cell. Next, we will fit the model to new datasets to assess how well it predicts.

5.2. Model testing and validation

To further evaluate the obtained BattX model, we generated new datasets by applying a variety of load profiles that span a range of currents. The first tests involved fully discharging the cell at a constant current of 0.5, 1, 4, and 5 C separately. Fig. 12 compares the BattX model’s prediction of the terminal voltage against the measurement, where a close match is observed in all four cases. Note that, even though the model was identified based on tests of only up to 3 C, it can well predict 4 C and 5 C, suggesting its high fidelity.

Further, we adopted the Urban Dynamometer Driving Schedule (UDDS) as a variable load profile and scaled it to be between -8 C and 5 C to validate the BattX model. Here, we desire to compare the BattX model against the popular Thevenin model with two RC pairs. To calibrate the 2RC Thevenin model, we utilize the same nonlinear OCV relationship shown in Fig. 7 and then use the 1 C constant-current discharging data to determine all its RC parameters. The validation result is shown in Fig. 13. The top figure in Fig. 13 illustrates the load profile, which includes both charging and discharging as well as a rest period. The voltage prediction of the BattX model, as shown in Fig. 13, closely follows the true voltage overall. A slight discrepancy appears at the end of the test when the cell is about to be depleted. This is likely because the radical changes of the internal resistance at low SoC and high temperature are hard to be thoroughly captured. By contrast, the 2RC Thevenin’s model gives a poor prediction, especially when the current load is above 1 C. Fig. 14 then demonstrates the comparison of the predicted surface temperature by the BattX model

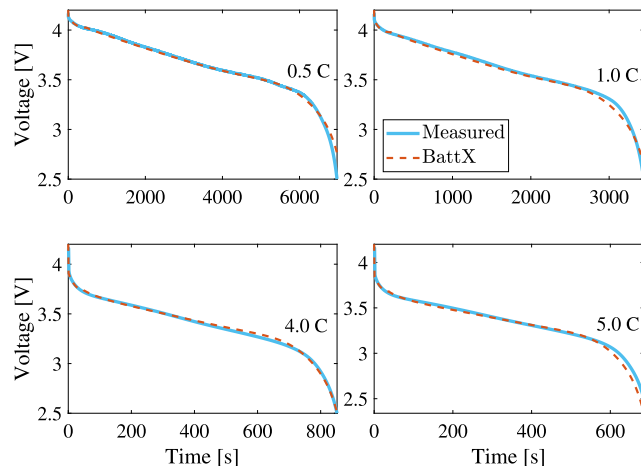


Fig. 12. Voltage prediction for constant-current discharging at 0.5, 1, 4, and 5 C.

with the measurement, showing an acceptable accuracy. The estimation of the core temperature is also given in Fig. 14, which is reasonable by empirical knowledge and observation.

Recently, LiB-powered eVTOL has attracted increasing interest as a promising solution to urban air mobility and decarbonization of aviation. A safety-critical application, eVTOL must maintain fast and accurate monitoring of its onboard battery system throughout a mission. Conventional equivalent circuit models are impossible to meet this need, as eVTOL often requires high-rate discharging—it must discharge as fast as 5 C in the takeoff and landing phases. However, the proposed BattX model holds a significant advantage to eVTOL battery performance modeling. We consider a notional eVTOL flight, which includes three phases, takeoff, cruising, and landing. The three phases involve discharging at 5 C, 1.48 C, and 5 C, respectively [34]. We generated a current load profile sequentially comprising a flight, full discharge, and another flight. Fig. 15 displays the current load profile over time and the voltage prediction by the BattX model and by the 2RC Thevenin model. It is seen that the BattX model achieves accurate prediction compared with the measurement. Especially, the accuracy is found satisfactory at times of high discharge rates. The 2RC Thevenin’s model, however, generates considerably larger prediction errors and finds itself struggling to capture the cell’s voltage behavior at high C-rates. These error magnitudes render the model far from sufficient for the eVTOL application. For the BattX model, the surface temperature prediction in Fig. 16 also well agrees with the actual temperature, and the core temperature estimation shows a real trend that one can trust to be close enough to the truth.

6. Conclusions

LiBs have found their way into many sectors as a key technology to drive forward electrification and decarbonization. For LiB applications, computationally fast and accurate ECMs are a bedrock for real-time monitoring and simulation to ensure their performance and safety. Although the literature has presented several different ECMs, none of them is effective when current loads range from low to high. To overcome the problem, we proposed the BattX model in this study. This model is an ECM in its form, but unlike other ECMs, it lends to interpretation as a quasi-electrochemical model. This is because it is designed to use separate yet coupled circuits to approximate the lithium-ion diffusion in the electrode and electrolyte phases, heat transfer, and nonlinear voltage behavior in charging/discharging of a cell. With this novel design, the model offers high predictive accuracy over broad current ranges and still retains relatively simple structures for low computational costs. We also developed a parameter identification

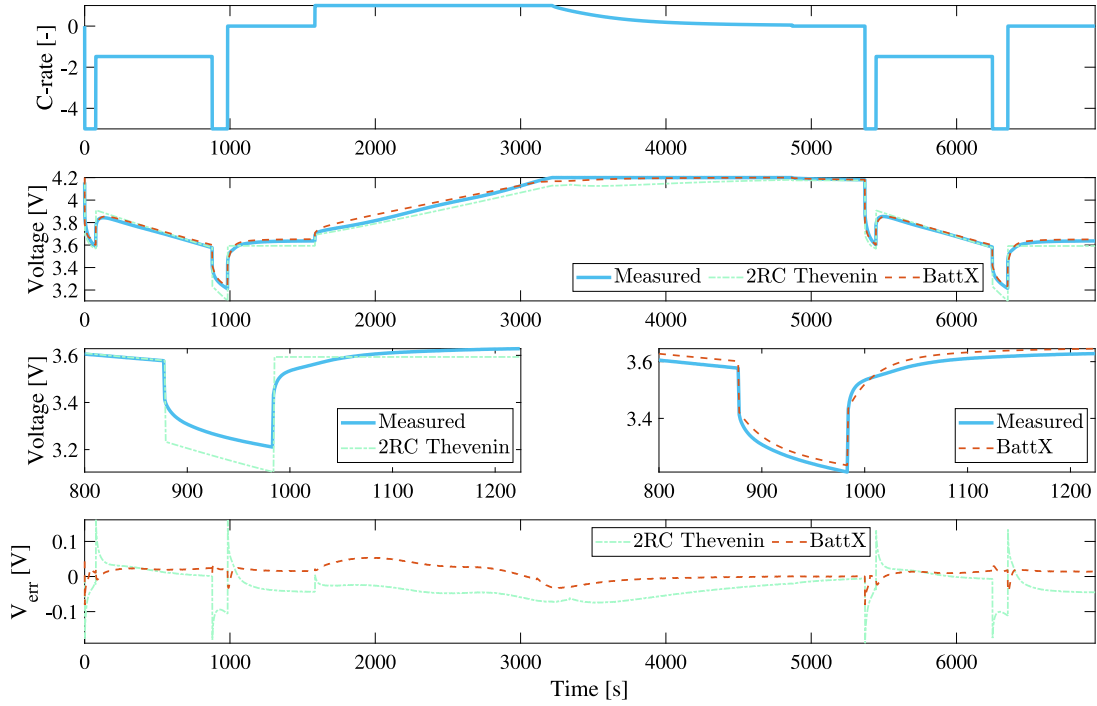


Fig. 15. BattX versus 2RC Thevenin's under an eVTOL profile. Row 1: the current load profile; row 2: the actual and predicted voltage; row 3: zoomed (left: 2RC Thevenin's; right: BattX); row 4: the voltage prediction error.

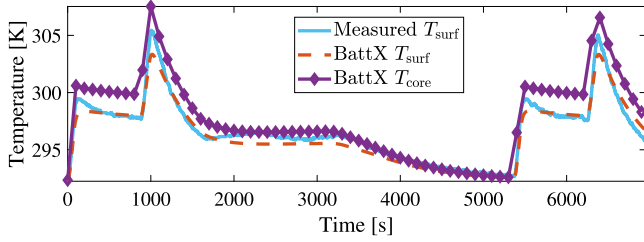


Fig. 16. Temperature prediction by the BattX model versus the measurements in the test simulating an eVTOL operation cycle.

$$B_s = \begin{bmatrix} \frac{1}{C_{s,1}} & 0 & \dots & 0 \end{bmatrix}^T.$$

The solution to (A.1) is given by

$$V_s(t) = e^{A_s t} V_s(0) + \int_0^t e^{A_s(t-\tau)} B_s I(\tau) d\tau.$$

When I is constant, it becomes

$$V_s(t) = e^{A_s t} V_s(0) + \int_0^t e^{A_s(t-\tau)} d\tau \cdot B_s I. \quad (\text{A.2})$$

To find the explicit form of $V_s(t)$, we must derive the expression of $e^{A_s t}$. To this end, we look at Ω_s first and note that it is rank-deficient with one zero eigenvalue. Further, assume the other non-zero eigenvalues to be distinct, and denote the eigenvalues of Ω_s as λ_i for $i = 1, 2, \dots, N$ with $\lambda_1 = 0$. Then, by the Cayley–Hamilton theorem, we have

$$e^{A_s t} = [\Phi^{-1} \phi(\mu_s, t)] \otimes \Omega_s, \quad (\text{A.3})$$

where

$$\Phi = \begin{bmatrix} 1 & \lambda_1 & \dots & \lambda_1^{N-1} \\ 1 & \lambda_2 & \dots & \lambda_2^{N-1} \\ \vdots & \vdots & \ddots & \vdots \\ 1 & \lambda_N & \dots & \lambda_N^{N-1} \end{bmatrix},$$

$$\phi(\mu_s, t) = [1 \quad e^{\mu_s \lambda_2 t} \quad \dots \quad e^{\mu_s \lambda_N t}]^T.$$

The operator \otimes is defined as

$$a \otimes A = \sum_{i=1}^n a_i A^{i-1},$$

for $a \in \mathbb{R}^{n \times 1}$ and $A \in \mathbb{R}^{n \times n}$. Inserting (A.3) into (A.6), we obtain

$$\begin{aligned} V_s(t) &= [\Phi^{-1} \phi(\mu_s, t)] \otimes \Omega_s \cdot V_s(0) + \int_0^t [\Phi^{-1} \phi(\mu_s, t - \tau)] \otimes \Omega_s d\tau \cdot B_s I \\ &= [\Phi^{-1} \phi(\mu_s, t)] \otimes \Omega_s \cdot V_s(0) + \left[\Phi^{-1} \int_0^t \phi(\mu_s, t - \tau) d\tau \right] \otimes \Omega_s \cdot B_s I \\ &= [\Phi^{-1} \phi(\mu_s, t)] \otimes \Omega_s \cdot V_s(0) + [\Phi^{-1} (\bar{\phi}(\mu_s, t) - \bar{\phi}(\mu_s, 0))] \otimes \Omega_s \cdot B_s I, \end{aligned} \quad (\text{A.4})$$

where

$$\bar{\phi}(\mu_s, t) = \begin{bmatrix} t & \frac{e^{\mu_s \lambda_2 t}}{\mu_s \lambda_2} & \dots & \frac{e^{\mu_s \lambda_N t}}{\mu_s \lambda_N} \end{bmatrix}^T.$$

Given (A.4), $V_{s,1}$ can be expressed as

$$V_{s,1}(t) = \mathbf{e}_1^T V_s(t),$$

where $\mathbf{e}_1 = [1 \quad 0 \quad \dots \quad 0]_{N \times 1}^T$.

Appendix B. Derivation of $V_{e,1}$ and $V_{e,3}$ under constant current I

The explicit expressions of $V_{e,1}$ and $V_{e,3}$ under a constant current I are needed to represent U_e for the identification of θ_e in (22). We can follow similar lines in Appendix A to find them out. Let us rewrite the governing equations of sub-circuit B in (2) compactly as

$$\dot{V}_e(t) = A_e V_e(t) + B_e I(t), \quad (\text{A.5})$$

where

$$\begin{aligned} V_e &= [V_{e,1} \quad V_{e,2} \quad V_{e,3}]^T, \\ A_e &= \mu_e \Omega_e, \\ \mu_e &= \frac{1}{C_e R_e}, \end{aligned}$$

$$\Omega_e = \begin{bmatrix} -1 & 1 & 0 \\ 1 & -2 & 1 \\ 0 & 1 & -1 \end{bmatrix},$$

$$B_e = \begin{bmatrix} \frac{1}{C_e} & 0 & -\frac{1}{C_e} \end{bmatrix}^T.$$

The solution to (A.5) under a constant current I is

$$V_e(t) = e^{A_e t} V_e(0) + \int_0^t e^{A_e(t-\tau)} d\tau \cdot B_e I. \quad (\text{A.6})$$

The eigenvalues of Ω_e are 0, -1, -3, respectively. By the Cayley–Hamilton theorem, it follows that

$$e^{A_e t} = [\Psi^{-1} \psi(\mu_e, t)] \otimes \Omega_e, \quad (\text{A.7})$$

where

$$\Psi = \begin{bmatrix} 1 & 0 & 0 \\ 1 & -1 & 1 \\ 1 & -3 & 9 \end{bmatrix},$$

$$\psi(\mu_e, t) = \begin{bmatrix} 1 & e^{-\mu_e t} & e^{-3\mu_e t} \end{bmatrix}^T.$$

Based on (A.7), we can derive that

$$V_e(t) = [\Psi^{-1} \psi(\mu_e, t)] \otimes \Omega_e \cdot V_e(0) + [\Psi^{-1} (\bar{\psi}(\mu_e, t) - \bar{\psi}(\mu_e, 0))] \otimes \Omega_e \cdot B_e I, \quad (\text{A.8})$$

where

$$\bar{\psi}(\mu_e, t) = \begin{bmatrix} t & -\frac{e^{-\mu_e t}}{\mu_e} & -\frac{e^{-3\mu_e t}}{3\mu_e} \end{bmatrix}^T.$$

With (A.8), one can extract $V_{e,1}$ and $V_{e,3}$ from V_e .

References

- [1] Plett GL. Battery management systems, Volume I: Battery modeling. Artech House; 2015.
- [2] Chaturvedi NA, Klein R, Christensen J, Ahmed J, Kojic A. Algorithms for advanced battery-management systems. *IEEE Control Syst Mag* 2010;30(3):49–68.
- [3] Wang Y, Fang H, Zhou L, Wada T. Revisiting the state-of-charge estimation for lithium-ion batteries: A methodical investigation of the extended Kalman filter approach. *IEEE Control Syst Mag* 2017;37(4):73–96.
- [4] Ramadesigan V, Northrop PWC, De S, Santhanagopalan S, Braatz RD, Subramanian VR. Modeling and simulation of lithium-ion batteries from a systems engineering perspective. *J Electrochem Soc* 2012;159(3):R31–45.
- [5] Doyle M, Fuller TF, Newman J. Modeling of galvanostatic charge and discharge of the lithium/polymer/insertion cell. *J Electrochem Soc* 1993;140(6):1526–33.
- [6] Ning G, Popov BN. Cycle life modeling of lithium-ion batteries. *J Electrochem Soc* 2004;151(10):A1584.
- [7] Guo M, Sikha G, White R. Single-particle model for a lithium-ion cell: Thermal behavior. *J Electrochem Soc* 2011;158(2):A122.
- [8] Tanim TR, Rahn CD, Wang C-Y. State of charge estimation of a lithium ion cell based on a temperature dependent and electrolyte enhanced single particle model. *Energy* 2015;80:731–9.
- [9] Khaleghi Rahimian S, Rayman S, White RE. Extension of physics-based single particle model for higher charge–discharge rates. *J Power Sources* 2013;224:180–94.
- [10] Moura SJ, Argomedo FB, Klein R, Mirtabatabaei A, Krstic M. Battery state estimation for a single particle model with electrolyte dynamics. *IEEE Trans Control Syst Technol* 2017;25(2):453–68.
- [11] Han X, Ouyang M, Lu L, Li J. Simplification of physics-based electrochemical model for lithium ion battery on electric vehicle. Part I: Diffusion simplification and single particle model. *J Power Sources* 2015;278:802–13.
- [12] Marquis SG, Sulzer V, Timms R, Please CP, Chapman SJ. An asymptotic derivation of a single particle model with electrolyte. *J Electrochem Soc* 2019;166(15):A3693.
- [13] Li J, Lotfi N, Landers RG, Park J. A single particle model for lithium-ion batteries with electrolyte and stress-enhanced diffusion physics. *J Electrochem Soc* 2017;164(4):A874–83.
- [14] Li J, Adewuyi K, Lotfi N, Landers R, Park J. A single particle model with chemical/mechanical degradation physics for lithium ion battery State of Health (SOH) estimation. *Appl Energy* 2018;212:1178–90.
- [15] Gopalakrishnan K, Offer GJ. A composite single particle lithium-ion battery model through system identification. *IEEE Trans Control Syst Technol* 2022;30(1):1–13.
- [16] Saccani G, Ciaramella G, Raimondo DM. A computationally efficient implementation of a battery pack electrochemical model using waveform relaxation. *J Energy Storage* 2022;46:103758.
- [17] Farmann A, Sauer DU. Comparative study of reduced order equivalent circuit models for on-board state-of-available-power prediction of lithium-ion batteries in electric vehicles. *Appl Energy* 2018;225:1102–22.
- [18] He H, Xiong R, Fan J. Evaluation of lithium-ion battery equivalent circuit models for state of charge estimation by an experimental approach. *Energies* 2011;4:582–98.
- [19] Mousavi G. S, Nikdel M. Various battery models for various simulation studies and applications. *Renew Sustain Energy Rev* 2014;32:477–85.
- [20] Tian N, Wang Y, Chen J, Fang H. One-shot parameter identification of the thevenin's model for batteries: Methods and validation. *J Energy Storage* 2020;29:101282.
- [21] Plett GL. Extended Kalman filtering for battery management systems of LiPB-based HEV battery packs: Part 2. Modeling and identification. *J Power Sources* 2004;134(2):262–76.
- [22] Lee K-T, Dai M-J, Chuang C-C. Temperature-compensated model for lithium-ion polymer batteries with extended Kalman filter state-of-charge estimation for an implantable charger. *IEEE Trans Ind Electron* 2018;65(1):589–96.
- [23] Chen M, Rincon-Mora G. Accurate electrical battery model capable of predicting runtime and I-V performance. *IEEE Trans Energy Convers* 2006;21(2):504–11.
- [24] Hu X, Li S, Peng H. A comparative study of equivalent circuit models for Li-ion batteries. *J Power Sources* 2012;198:359–67.
- [25] Weng C, Sun J, Peng H. A unified open-circuit-voltage model of lithium-ion batteries for state-of-charge estimation and state-of-health monitoring. *J Power Sources* 2014;258:228–37.
- [26] Tian N, Fang H, Chen J, Wang Y. Nonlinear double-capacitor model for rechargeable batteries: Modeling, identification, and validation. *IEEE Trans Control Syst Technol* 2020;29(1):370–84.
- [27] Tian N, Fang H, Chen J. A new nonlinear double-capacitor model for rechargeable batteries. In: *Proceedings of the 44th annual conference of the IEEE industrial electronics society*. 2018, p. 1613–8.
- [28] Movahedi H, Tian N, Fang H, Rajamani R. Hysteresis compensation and nonlinear observer design for state-of-charge estimation using a nonlinear double-capacitor li-ion battery model. *IEEE/ASME Trans Mechatronics* 2022;27(1):594–604.
- [29] Li AG, Mayilvahanan K, West AC, Preindl M. Discrete-time modeling of Li-ion batteries with electrochemical overpotentials including diffusion. *J Power Sources* 2021;500:229991.
- [30] Fan C, O'Regan K, Li L, Higgins MD, Kendrick E, Widanage WD. Data-driven identification of lithium-ion batteries: A nonlinear equivalent circuit model with diffusion dynamics. *Appl Energy* 2022;321:119336.
- [31] Xi Z, Dahmardeh M, Xia B, Fu Y, Mi C. Learning of battery model bias for effective state of charge estimation of lithium-ion batteries. *IEEE Trans Veh Technol* 2019;68(9):8613–28.
- [32] Tu H, Moura S, Wang Y, Fang H. Integrating physics-based modeling with machine learning for lithium-ion batteries. *Appl Energy* 2023;329:120289.
- [33] Hu Y, de Callafon RA, Tian N, Fang H. Tensor network-based MIMO Volterra model for lithium-ion batteries. *IEEE Trans Control Syst Technol* 2023. (in press).
- [34] Bills A, Sripad S, Fredericks WL, Guttenberg M, Charles D, Frank E, et al. Universal battery performance and degradation model for electric aircraft. 2020, arXiv preprint arXiv:2008.01527.
- [35] Lin X, Perez H, Mohan S, Siegel J, Stefanopoulou A, Ding Y, et al. A lumped-parameter electro-thermal model for cylindrical batteries. *J Power Sources* 2014;257:1–11.
- [36] Mehta R, Gupta A. An improved single-particle model with electrolyte dynamics for high current applications of lithium-ion cells. *Electrochim Acta* 2021;389:138623.
- [37] Moura SJ, Argomedo FB, Klein R, Mirtabatabaei A, Krstic M. Battery state estimation for a single particle model with electrolyte dynamics. *IEEE Trans Control Syst Technol* 2016;25(2):453–68.
- [38] Fang H, Wang Y, Chen J. Health-aware and user-involved battery charging management for electric vehicles: Linear quadratic strategies. *IEEE Trans Control Syst Technol* 2017;25(3):911–23.
- [39] Xu X, Wang W, Chen L. Order reduction of lithium-ion battery model based on solid state diffusion dynamics via large scale systems theory. *J Electrochem Soc* 2016;163(7):A1429–41.